

New XMM-Newton observation of the Phoenix cluster: properties of the cool core

P. Tozzi¹, F. Gastaldello², S. Molendi², S. Ettori^{3,4}, J. S. Santos¹, S. De Grandi⁵, I. Balestra⁶, P. Rosati^{7,1}, B. Altieri⁸, G. Cresci¹, F. Menanteau^{9,10}, I. Valtchanov⁸

¹ INAF, Osservatorio Astrofisico di Firenze, Largo Enrico Fermi 5, I-50125, Firenze, Italy

² INAF, IASF Milano, via E. Bassini 15 I-20133 Milano, Italy

³ INAF, Osservatorio Astronomico di Bologna, viale Berti Pichat 6/2, I-40127 Bologna, Italy

⁴ INFN, Sezione di Bologna, viale Berti Pichat 6/2, I-40127 Bologna, Italy

⁵ INAF, Osservatorio Astronomico di Brera, via E. Bianchi 46, I-23807 Merate, Italy

⁶ INAF, Osservatorio Astronomico di Trieste, via G.B. Tiepolo 11, I-34131, Trieste, Italy

⁷ Università degli Studi di Ferrara, Via Savonarola, 9 - 44121 Ferrara, Italy

⁸ European Space Astronomy Centre (ESAC), European Space Agency, Apartado de Correos 78, 28691 Villanueva de la Cañada, Madrid, Spain

⁹ National Center for Supercomputing Applications, University of Illinois at Urbana-Champaign, 1205 W. Clark St., Urbana, IL 61801, USA

¹⁰ Department of Astronomy, University of Illinois at Urbana-Champaign, W. Green Street, Urbana, IL 61801, USA

May 21, 2015

ABSTRACT

Aims. We present a spectral analysis of a deep (220 ks) XMM-Newton observation of the Phoenix cluster (SPT-CL J2344-4243), which we also combine with *Chandra* archival ACIS-I data, particularly useful to model the central bright AGN and global ICM properties.

Methods. We extract CCD and RGS X-ray spectra from the core region to search for the signature of cold gas, and, ultimately, constrain the mass deposition rate in the cooling flow which is thought to be responsible of the massive star formation episode observed in the BCG.

Results. We find an average mass deposition rate of $\dot{M} = 620(-190 + 200)_{\text{stat}}(-50 + 150)_{\text{syst}} M_{\odot} \text{ yr}^{-1}$ in the temperature range 0.3-3.0 keV from MOS data. A temperature-resolved analysis shows that a significant amount of gas is deposited only at about 1.8 keV and above, while only upper limits of the order of hundreds of $M_{\odot} \text{ yr}^{-1}$ can be put in the 0.3-1.8 keV temperature range. From pn data we obtain $\dot{M} = 210(-80 + 85)_{\text{stat}}(-35 + 60)_{\text{syst}} M_{\odot} \text{ yr}^{-1}$ in the 0.3-3.0 keV temperature range, while the upper limits from the temperature-resolved analysis are typically a factor of 3 lower than MOS data. In the RGS spectrum, no line emission from ionization states below Fe XXIII is seen above 12Å, and the amount of gas cooling below ~ 3 keV has a formal best-fit value $\dot{M} = 122^{+343}_{-122} M_{\odot} \text{ yr}^{-1}$. In addition, our analysis of the FIR SED of the BCG based on *Herschel* data provides $SFR = 530 M_{\odot} \text{ yr}^{-1}$ with an uncertainty of 10%, significantly lower than previous estimates by a factor 1.5. Overall, current limits on the mass deposition rate from MOS data are consistent with the star formation rate observed in the BCG, while pn data prefer a lower value $\dot{M} \sim SFR/3$, inconsistent with the SFR at the 3σ c.l.

Conclusions. Current data are able to firmly identify substantial amount of cooling gas only above 1.8 keV in the core of the Phoenix cluster. At lower temperatures, the upper limits on \dot{M} from MOS and pn data differ by a factor of 3. While MOS data analysis is consistent with values as high as $\dot{M} \sim 1000$ within 1σ , pn data provide $\dot{M} < 500 M_{\odot} \text{ yr}^{-1}$ at 3σ c.l. at temperature below 1.8 keV. At present, this discrepancy cannot be explained on the basis of known calibration uncertainties or other sources of statistical noise.

Key words. galaxies: clusters: individual: SPT-CL J2344-4243 – intracluster medium; X-ray: galaxies: clusters

1. Introduction

The majority of baryons in clusters of galaxies is constituted by virialized hot gas (Lin et al. 2003; Gonzalez et al. 2013) that emits X-ray via thermal bremsstrahlung. Temperature, density and chemical composition of the so-called Intra Cluster Medium (ICM) can be directly measured thanks to X-ray imaging and spectroscopic observations. Spatially resolved spectroscopic studies showed the presence of significant temperature decrease and strongly peaked surface brightness profiles in the center of a significant fraction of the cluster population. The short cooling times associated to these high-density gas regions,

led to the conclusion that a massive cooling flow was developing in the ICM in most of the clusters (Silk 1976; Cowie & Binney 1977; Fabian & Nulsen 1977; Mathews & Bregman 1978). The fate of this cooling gas would be to feed massive star formation episodes.

On the basis of the isobaric cooling flow model (Fabian & Nulsen 1977; Fabian 1994), it was estimated that typical cooling flows may develop mass deposition rates in the range of a few $\times 100 - 1000 M_{\odot} \text{ yr}^{-1}$. However, the lack of massive star formation events and of large reservoirs of cold gas at the center of galaxy clusters casted some doubts on the hypothesis of a complete cooling of the ICM in cluster cores. The picture changed dramatically when X-ray observations, in particular the RGS instrument onboard of the XMM-

Newton telescope, revealed a severe deficit of emission lines compared to the predictions of the isobaric cooling–flow model in all the groups and clusters of galaxies with putative cooling flows (Tamura et al. 2001; Peterson et al. 2001; Kaastra et al. 2001; Peterson et al. 2003). Interestingly, this result has been found also in XMM-Newton and *Chandra* CCD spectra, despite the lower resolution, thanks to the prominent complex of iron L-shell lines (McNamara et al. 2000; Böhringer et al. 2001; Molendi & Pizzolato 2001; Böhringer et al. 2002). This directly implies that the cooling gas is present only in small amounts, typically 10 times lower than expected in the case of a steady-state, isobaric radiative cooling (see Peterson & Fabian 2006). This determined a change from the cooling-flow paradigm, with typical deposition rates of the order of $100 - 1000 M_{\odot} \text{ yr}^{-1}$, to the cool-core paradigm, where most of the gas is kept at temperatures larger than 1/3 of the ambient cluster temperature, and the mass deposition rate, if any, is due to a residual cooling flow of the order of few tens $M_{\odot} \text{ yr}^{-1}$.

Another direct implication of these observations is the existence of some process that heats the gas and prevents its cooling. Among the many mechanisms investigated in the last years, AGN feedback is considered the most plausible heating source. Radio AGN are ubiquitous in cool cores (see Sun 2009) and interactions between the radio jets and the ICM have been clearly observed. AGN outbursts in principle can inject sufficient amount of energy into the ICM (see McNamara et al. 2005). The relativistic electrons in jets associated to the central cluster galaxy are able to carve large cavities into the ICM. The free energy associated to these "bubbles" is plausibly transferred into the ICM and thermalized through turbulence (see McNamara & Nulsen 2012; Zhuravleva et al. 2014). In addition, there are increasing evidence of interactions of AGN outflows with metal-rich gas along the cavities and edges of radio jets of some individual clusters and groups (Kirkpatrick et al. 2011; Ettori et al. 2013b), consistent with numerical simulations showing that AGN outflows are able to advect ambient, iron-rich material from the core to few hundreds kpc away (e.g., Gaspari et al. 2011a,b). The feedback mechanism has been observed in its full complexity in nearby clusters like Perseus (Fabian et al. 2003, 2006, 2011), Hydra A (McNamara et al. 2000), and a few other clusters (see Blanton et al. 2011).

In addition, the regular behaviour of cool cores is not only observed in local clusters, but it seems to hold up to high redshifts. High angular resolution observations of cool cores at $z \leq 1$ performed by our group (Santos et al. 2010, 2012) showed that the radio feedback mechanism is already present at $z \sim 1$. Temperature and metallicity profiles in cool cores are broadly consistent with local ones, with a remarkable difference in the metal distribution which appear to be more concentrated in the core than local clusters (De Grandi et al. 2014), indicating a role of the radio feedback also in the spatial distribution of metals. The regularity of the cool-core appearance over the entire cluster population and a large range of epochs, points towards a gentle heating mechanism, with the radio AGN acting with a short duty cycle in order to counterbalance the onset of cooling flows since the very first stages of cluster formation. At the same time, outburst shocks may provide a more violent heating mechanism. Whether AGN heating of the ICM occurs violently through shocks or through bubbles in pressure equilibrium causing turbulence, is poorly understood. Outburst shock with jumps in temperature are very hard to detect, and the presence of shocks has been clearly found only in a few cases (see, e.g., A2052 and NGC5813, Blanton et al. 2011; Randall et al. 2011). In any case, it is now widely accepted that the mechanical energy provided

by the AGN through jets is sufficient to overcome the cooling process in cluster cores. Therefore, the detailed physical mechanism that transfers energy to the ICM, and how this mechanism gives rise the regular cool-core thermal structure, with a minimum temperature a factor ~ 3 lower than the ambient cluster temperature, are still open issues.

Surprisingly, a recent observation introduced further changes in the picture outlined here. The SZ-selected cluster SPT-CLJ2344-4243 (also known as the Phoenix cluster, McDonald et al. 2012) at $z \sim 0.56$, shows for the first time hints of a massive cooling-flow-induced starburst, suggesting that the feedback source responsible for preventing runaway cooling may not be fully established yet. SPT-CLJ2344-4243 shows a strong cool core with a potential mass deposition rate of $\sim 3000 M_{\odot} \text{ yr}^{-1}$ derived from the X-ray luminosity. McDonald et al. (2012) argued that the Phoenix cluster actually harbors an almost isobaric cooling flow with an unusually large mass deposition rate. The strongest hint comes from the very high star formation rate (SFR) observed in the BCG, which has been originally estimated to be $\sim 700 M_{\odot} \text{ yr}^{-1}$, with large 1σ errors ranging from 200 to $500 M_{\odot} \text{ yr}^{-1}$ (McDonald et al. 2012). However, an accurate measurement of the SFR is made difficult by the presence of a strongly absorbed AGN, whose contribution to the BCG emission can be accounted for in different ways. Recently, the HST/WFC3 observation of the Phoenix (McDonald et al. 2013) showed filamentary blue emission out to 40 kpc and beyond, and the estimated, extinction-corrected SFR has been updated to a more accurate value of $798 \pm 42 M_{\odot} \text{ yr}^{-1}$, consistent with optical and IR data at lower spatial resolution.

In this work we present the analysis of a 220 ks observation with XMM-Newton awarded in AO12 on the Phoenix cluster, with the main goal of investigating the thermal structure of the cool core, and to compare the mass deposition rate in the core to the star formation rate in the BCG. We also use archival *Chandra* data (about 10 ks with ACIS-I) to model the emission of the AGN in the BCG and global ICM properties. Finally, we revise the SFR in the BCG on the basis of FIR data from the *Herschel* Observatory.

The paper is organized as follows. In §2 we will describe the data reduction of the XMM-Newton and *Chandra* data. In §3 we present the results from the *Chandra* data analysis on the central AGN spectrum and the global ICM properties. In §4 we describe our analysis strategy and present the results on the cool core temperature structure from EPIC MOS and pn data, RGS data, and also *Chandra* data. In §5 we revise the measurement of the star formation rate in the BCG from FIR data in view of a comparison with the mass deposition rate. Finally our conclusions are summarized in §6. Throughout the paper, we adopt the seven-year WMAP cosmology with $\Omega_{\Lambda} = 0.73$, $\Omega_m = 0.27$, and $H_0 = 70.4 \text{ km s}^{-1} \text{ Mpc}^{-1}$ (Komatsu et al. 2011). Quoted errors and upper limits always correspond to a 1σ confidence level, unless stated otherwise.

2. Data reduction

2.1. XMM-Newton: EPIC data

We obtained a total of 225 ks with XMM-Newton on the Phoenix cluster in AO12¹. Data were acquired in November and December 2013 (Obsid 0722700101, 132 ks, and 0722700201,

¹ Proposal ID 72270, "The thermal structure of the cool core in the Phoenix cluster", PI P. Tozzi

Table 1. XMM-Newton data: exposure times for each Obsid after data reduction.

Obsid	EPIC detector	effective t_{exp} ks
0722700101	MOS1	128.0
0722700101	MOS2	128.0
0722700101	pn	103.0
0722700201	MOS1	92.0
0722700201	MOS2	92.0
0722700201	pn	81.5
0693661801	MOS1	16.0
0693661801	MOS2	16.5
0693661801	pn	8.6

93 ks). We add to our analysis a shorter 20 ks archival observation taken in 2012.²

The observation data files (ODF) were processed to produce calibrated event files using the most recent release of the XMM-Newton Science Analysis System (SAS v14.0.0), with the calibration release XMM-CCF-REL-323, and running the tasks EPPROC and EMPROC for the pn and MOS, respectively, to generate calibrated and concatenated EPIC event lists. Then, we filter EPIC event lists for bad pixels, bad columns, cosmic rays events outside the FOV, photons in the gaps (FLAG=0), and apply standard grade selection, corresponding to PATTERN < 12 for MOS and PATTERN <= 4 for pn. We removed soft proton flares by applying a threshold on the count rate in the 10–12 keV energy band. To define low background interval we use the condition $RATE \leq 0.35$ for MOS and $RATE \leq 0.4$ for pn. We find that for Obsid 0722700101, after data reduction we have about 128 ks for MOS1 and MOS2 and 103 ks for pn. For Obsid 0722700201 we have 92 ks for MOS1 and MOS2 and 81.5 ks for pn. Therefore, the removal of high background intervals reduces the effective time from 225 ks to 220 for MOS (a loss of 2% of the total time) and to 184.5 ks for pn (a loss of 18% of the total time). The archival data, Obsid 0693661801, were affected by flares by a larger amount. From 20 ks of exposure in Obsid 0693661801, we have 16 and 16.5 ks for MOS1 and MOS2, respectively (a loss of about 18–20%), and 8.6 ks for pn (a loss of about 60% of the total time).

For each Obsid we merge the event files MOS1 and MOS2 to create a single event file. This procedure has been adopted since the MOS cameras yield typically mutually consistent fluxes over their whole energy bandpass³. Finally, we also removed out-of-time events from the pn event file and spectra. In Table 1, we list the resulting clean exposure times for the pn and the MOS detectors for the three exposures used in this work.

Effective area and response matrix files are generated with the tasks `arfgen` and `rmfgen`, respectively, for each obsid. In the case of MOS, effective area and response matrix files are computed for each detector and eventually summed with a weight corresponding to the effective exposure time of MOS1 and MOS2.

2.2. XMM-Newton: RGS data

We reduced the RGS data set using the standard SAS v14.0.0 pipeline processing through the RGSPROC tool. We filter soft proton flares by excluding time periods where the count rate on CCD9⁴ is less than 0.1 cts/s in a region free of source emission. The resulting effective exposure times, after removing flares from the data, are listed in Table 2. As background we adopted the model background spectrum created by the SAS task RGSBKGMODEL which can be applied to a given observation from a combination of observations of empty fields, based on the count rate of the off-axis, source-free region of CCD9. We double checked that the background spectrum in this way obtained is entirely consistent with a local background extracted from beyond 98% of the RGS PSF. Finally, we focus on the first order spectra and combine spectra, backgrounds and responses from all observations and from both RGS instruments using the SAS task RGScombine.

Table 2. Cleaned exposure times for RGS detectors

Obsid	RGS detector	effective t_{exp} ks
0722700101	RGS1	126.4
0722700101	RGS2	125.2
0722700201	RGS1	92.4
0722700201	RGS2	92.7

2.3. Archival Chandra data

The Phoenix cluster has been observed with ACIS-I for 11.9 ks in the VFAINT mode (Obsid 13401)⁵. We performed a standard data reduction starting from the level=1 event files, using the CIAO 4.6 software package, with the most recent version of the

⁴ This is the CCD that generally records the least source events due to its location close to the optical axis and is the most susceptible to proton events.

⁵ Proposal ID 13800933, "Chandra Observation of the Most Massive Galaxy Clusters Detected in the South Pole Telescope Survey", PI. G. Garmire.

² Proposal ID 069366, PI M. Arnaud.

³ See <http://xmm2.esac.esa.int/docs/documents/CAL-TN-0018.pdf>.

Chandra Calibration Database (CALDB 4.6.3). We ran the task `acis_process_events` to flag background events that are most likely associated with cosmic rays and remove them. With this procedure, the ACIS particle background can be significantly reduced compared to the standard grade selection. The data is filtered to include only the standard event grades 0, 2, 3, 4 and 6. We visually checked for hot columns left after the standard reduction. As expected for exposures taken in VFAINT mode, we do not find hot columns or flickering pixels after filtering out bad events. Finally, we filter time intervals with high background by performing a 3σ clipping of the background level using the script `analyze_ltcrv`. Only a negligible fraction of the exposure time is lost in this step, and the final effective exposure time is 11.7 ks. We remark that our spectral analysis will not be affected by possible undetected flares, since we are able to compute the background in the same observation from a large, source-free region close to the cluster position, thus taking into account any possible spectral distortion of the background itself induced by the flares.

3. Spectral analysis of *Chandra* data: AGN spectrum and global ICM properties

We first perform the spectral analysis of the *Chandra* data. Despite the short exposure time⁶, the high angular resolution of *Chandra* can provide important parameters which will be used in the spectral analysis of the XMM-Newton data. In particular, from the high-resolution, hard-band image it is immediately clear that the BCG of the Phoenix cluster hosts a powerful obscured AGN. In XMM-Newton data, the point spread function has an half energy width (HEW) of about 15" at the aimpoint, which causes the AGN emission to be spread over the entire starburst region. *Chandra* data allow us to accurately measure the spectrum of the central AGN and eventually model its emission in the analysis of the XMM data.

We extract a circular region with a radius of 1.5 arcsec to analyze the position of the central source in the hard-band *Chandra* image ($RA = 23:44:43.9$, $DEC = -42:43:12.64$). At variance with the large majority of cool core clusters, the AGN in the center of the Phoenix is extremely X-ray luminous. We consider only the energy range 1.0-10 keV for fitting purpose to avoid residual contamination from the thermal emission of the ICM. We detect 575 net counts in the 1.0-7 keV band, most of them in the hard 2-7 keV band. In our fit we fix the redshift to the optical value $z_{opt} = 0.592$ (see McDonald et al. 2012). We also fix the Galactic absorption to the value $NH_{Gal} = 1.52 \times 10^{20} \text{ cm}^{-2}$ obtained from radio map of Kalberla et al. (2005) at the position of the cluster. The AGN is modeled as a power law with an intrinsic absorption (*XSPEC* model `zwabs` \times `pow`) convolved by the Galactic absorption model (`tbabs`). The slope of the power law is frozen to the value $\Gamma = 1.8$.

We find an intrinsic absorption $NH = (46 \pm 7) \times 10^{22} \text{ cm}^{-2}$ and unabsorbed intrinsic luminosities of $(3.1 \pm 0.1) \times 10^{45}$ and $(4.8 \pm 0.2) \times 10^{45} \text{ erg s}^{-1}$ in the 0.5-2 keV and 2-10 keV bands, respectively. The *Chandra* spectrum of the AGN and the best-fit model are shown in Figure 2. Therefore the central AGN can be classified as a Type II QSO. These results are consistent with the results of Ueda et al. (2013), who find $NH = (32 \pm 9) \times 10^{22} \text{ cm}^{-2}$ and $\Gamma = 1.54 \pm 0.27$ from the combined analysis of Suzaku XIS and HXD and *Chandra* (with CALDB 4.5.3). We also notice that if we leave Γ free in our fit, we find a much flatter spectrum

with an intrinsic absorption lower by a factor of two, in agreement with the findings of Ueda et al. (2013) for the *Chandra* data only, due to the well known degeneracy between spectral slope and intrinsic absorption. Given the very low value ~ 0.6 for the intrinsic spectral slope obtained in this way, we prefer to rely on the results with $\Gamma = 1.8$ consistent with the *Suzaku+Chandra* analysis. Since the contribution of the AGN in the soft band will be crucial in our spectral analysis of the core region, we eventually will allow NH to range from 23 to $53 \times 10^{22} \text{ cm}^{-2}$, to span the upper and lower 1σ limits of the two measurements in the analysis of the XMM data. Finally, we notice that we are not able to clearly identify the neutral Fe line at 6.4 keV rest-frame when adding an unresolved line component. We also remark that our analysis of *Chandra* data has been obtained by removing the surrounding ICM emission, and not modelling the thermal and AGN components together as in Ueda et al. (2013).

The total ICM emission contributes about 6400 net counts in the 0.5-7 keV, within a radius of about 650 kpc, beyond which the surface brightness reaches the background level. Therefore, we are able to perform the spectral analysis in independent rings with slightly less than 1000 net counts each. The projected temperature and iron abundance profiles are shown in Figure 1 in the left and right panels, respectively. The temperature profile clearly shows the presence of a prominent cool core with a decrease of at least a factor of 2 from 200 kpc to the inner 50 kpc. This is mirrored in the iron abundance profile as a clear peak towards the center, where the iron abundance reaches the solar metallicity (with solar metallicity values measured by Asplund et al. 2005) with an uncertainty of 30%. These results will be used to complement the spectral analysis of XMM-Newton data.

We also compute the deprojected temperature and density profiles with a backward method (see Ettori et al. 2010, 2013a), which makes use of the geometrically-deprojected X-ray surface brightness and temperature profiles to reconstruct the hydrostatic mass profile. This is assumed to be described by the NFW functional form (Navarro et al. 1996). The best-fit parameters of the mass profile are obtained through the minimization of the χ^2 statistics defined as the sum of the squared differences between the observed temperature and the temperature estimates obtained by inverting the equation of the hydrostatic equilibrium, weighted by the observational errors on the spectroscopic temperature. The gas density is derived from the deprojected surface brightness and the total mass model. With this method we measure a total mass, under the assumption of hydrostatic equilibrium, of $M_{500} = (2.34 \pm 0.71) \times 10^{15} M_{\odot}$ at $R_{500} = 1627 \pm 235$ kpc. The ICM mass within R_{500} is $M_{ICM} = (2.1 \pm 0.2) \times 10^{14} M_{\odot}$. Therefore we obtain an ICM fraction of $f_{ICM} = 0.09 \pm 0.03$ at R_{500} . As a simple check, we estimate the parameter $Y_X = (27.3 \pm 4.1) \times 10^{14} \text{ keV } M_{\odot}$ assuming as representative of the entire cluster the temperature measured between 100 and 500 kpc, and compute the mass estimate from Y_X assuming the relation described in Arnaud et al. (2010) with the slope fixed to the self-similar value. We find a mass of $(2.15 \pm 0.24) \times 10^{15} M_{\odot}$, consistent with the value previously computed from the hydrostatic equilibrium well within 1σ .

If we extrapolate the measured profile up to the virial radius adopting the best-fit NFW profile (Navarro et al. 1996) we find $M_{200} = 3.4 \pm 1.2 \times 10^{15} M_{\odot}$ at $R_{200} = 2500 \pm 400$ kpc. Note that this value is about a factor of 2 larger than the mass estimate $M_{200SZ} = (1.66 \pm 0.23_{\text{stat}} \pm 0.44_{\text{syst}}) \times 10^{15} M_{\odot}$ obtained from SZ-mass scaling relations in Williamson et al. (2011). However, considering that SZ-inferred masses are found to be statistically lower by a factor of 0.78 in their sample, the discrepancy be-

⁶ A new, 100 ks observation with *Chandra* has been taken in August 2014, PI M. McDonald.

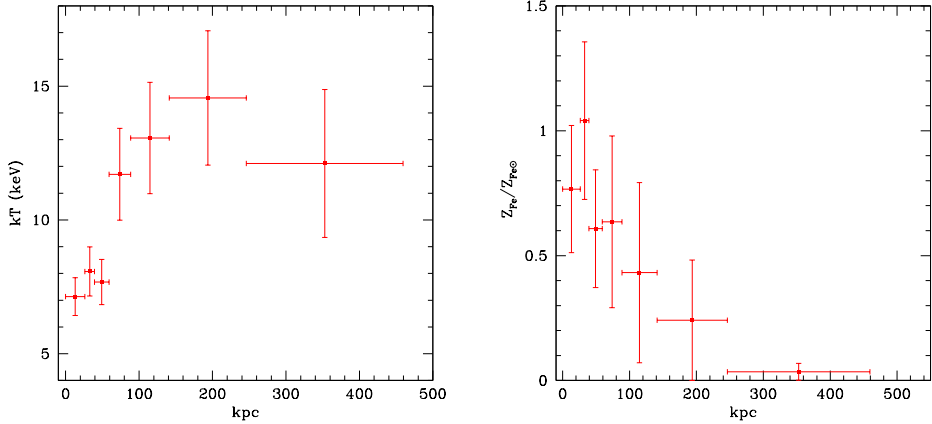


Fig. 1. *Left panel:* projected temperature profile of SPT-CLJ2344 obtained from the 11.7 ks *Chandra* ACIS-I observation, after removing the central AGN. Errorbars correspond to 1σ . *Right panel:* projected iron abundance profile of SPT-CLJ2344 from *Chandra* data.

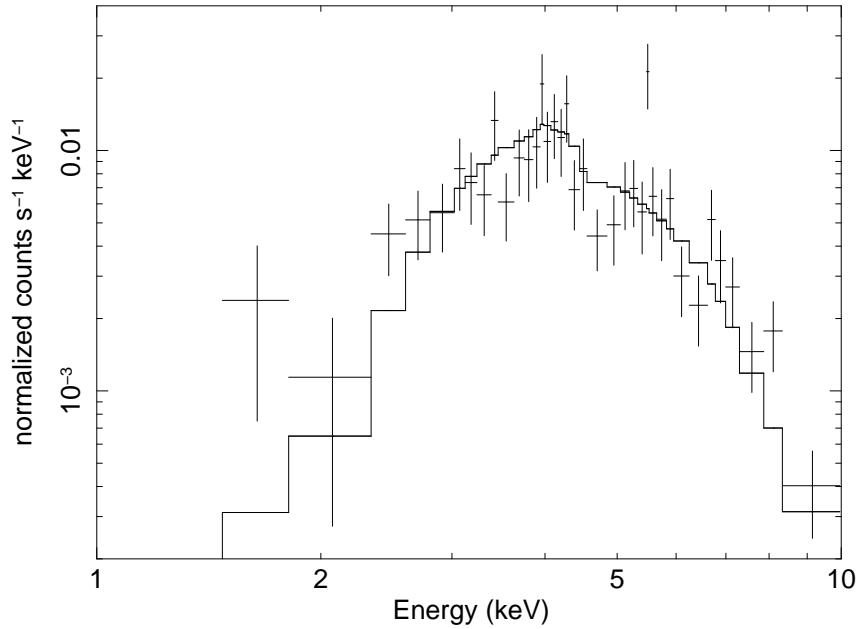


Fig. 2. Folded spectrum with best fit model for the AGN in the center of the BCG of the Phoenix cluster. The spectrum is extracted from a radius of only 1.5 arcsec centered on the peak of the hard X-ray emission.

tween X-ray and SZ mass for the Phoenix is reduced to $\sim 1\sigma$, and therefore is not significant. Finally, by extrapolating the ICM density distribution we find $M_{\text{ICM}} = (3.2 \pm 0.3) \times 10^{14} M_\odot$, for a virial ICM fraction of $f_{\text{ICM}} = 0.095 \pm 0.035$.

4. Spectral analysis of XMM-Newton data

4.1. Analysis strategy

We extract the spectra from a circular region with a radius of 13.5 arcsec. This region has been chosen in order to include the bulk of the emission from the core region, estimated to be confined within a radius of 40 kpc (about 6 arcsec at $z \sim 0.6$), plus 7.5 arcsec corresponding to the half-power diameter of the XMM-Newton PSF. Since the cold gas is expected to be concen-

trated towards the center of the cluster, we assume that the signal from the cold gas emission outside this radius is negligible. This assumption is consistent with the results we obtained from the RGS spectra in two different extraction regions (see §4.3).

The background is sampled from a nearby region on the same CCD free from the cluster emission, and it is subtracted from the source spectrum. We note that the total background expected in the source region, computed by rescaling geometrically the sampled background to the source area, amounts only to 0.3% of the total observed emission. Before performing the final spectral analysis, we run a few spectral fits artificially enhancing the background by factors of the order 1.2–1.5, a range which encompasses any possible uncertainty in the background level. We find no relevant differences in the best-fit values as a function of the background rescaling factor. We conclude that

the background has a small impact on the spectral analysis, and therefore, in the paper we will consider only the results obtained with the background sampled from the data and geometrically rescaled to the source region.

In XMM-Newton spectra the emission from the central AGN is mixed with the ICM emission, therefore we model its contribution with a power law spectrum with a fixed slope of $\Gamma = 1.8$ and an intrinsic absorption ranging from 23 to $53 \times 10^{22} \text{ cm}^{-2}$ at the redshift of the cluster, as found in §3. Also the normalization is left free for each separate spectrum to account for possible differences in the calibration of *Chandra* and XMM-Newton. We always find values in the range $(1.0 - 1.4) \times 10^{-3}$ for the normalization of the power law component. The Galactic absorption, instead, is frozen to the value $NH_{Gal} = 1.52 \times 10^{20} \text{ cm}^{-2}$ obtained from radio map of Kalberla et al. (2005) at the position of the cluster, and it is described by the `tbabs` model. The effects of possible uncertainties on the Galactic absorption are discussed together with other systematic effects in §4.4.

We assume that the gas in the residual cooling flow can be described by isobaric cooling model, therefore we use the `mkcflow` spectral model (Mushotzky & Szymkowiak 1988). This model assumes a unique mass deposition rate throughout the entire temperature range T_{min} - T_{max} . Since we are interested in the gas which is completely cooling continuously distributed across the entire temperature range, we set $T_{min} = 0.3 \text{ keV}$ and $T_{max} = 3.0 \text{ keV}$. We set the lowest temperature to 0.3 keV because this is the minimum value that can possibly contribute to the emission in the *Chandra* and XMM-Newton energy range, given the relatively high redshift of the Phoenix cluster. However, a single `mkcflow` model may not be sufficient to investigate the structure of the cool core. The actual situation may be more complex, with some of the gas, above a given temperature threshold, cooling at a relatively high rate consistent with the isobaric cooling flow model, while colder gas may have much lower mass deposition rate. Indeed, grating spectra of cool cores are traditionally fitted with an isobaric cooling flow model with a cutoff temperature below which no gas is detected (Peterson & Fabian 2006). To explore a more complex scenario, we aim at measuring the cooling rate (i.e., the mass deposition rate) in several temperature bins separately. In this case the temperature intervals are fixed to 0.3-0.45, 0.45-0.9, 0.9-1.8 and 1.8-3.0 keV. This choice is similar to use single-temperature `mekal` model for a discrete set of temperatures, but with the advantage of a continuous description of the gas instead of a set of discrete temperature values.

The contribution of the much hotter ICM component along the line of sight is modeled with a `mekal` model with a free temperature. Indeed, above 3 keV, a single temperature `mekal` model can account for the presence of several hot components, since it is not possible to resolve the temperature structure above 3 keV with the spectral analysis (see Mazzotta et al. 2004). This means that the possible contributions to the emission from temperatures between 3.0 keV (the maximum temperature of the `mkcflow`) and the best-fit temperature of the `mekal` model, are already described by a single-temperature `mekal` component. Therefore, despite the presence of a strong temperature gradient towards the center, the relevant part of the thermal structure of the ICM is properly treated by assuming a single temperature for the hot component, and exploring the low-temperature regime with a multi temperature `mkcflow` model.

In practice, our fitting method consists of two measurements of the mass deposition rates, using the following models:

- a single cooling-flow model `mkcflow` plus one single-temperature `mekal` component. The lowest temperature of the `mkcflow` component is frozen to 0.3 keV, and the largest to 3.0 keV. By setting the minimum temperature to 0.3 keV, we can interpret the normalization of the `mkcflow` model as the global deposition rate allowed for an isobaric cooling flow across the entire 0.3-3.0 keV temperature range. The redshift is tied to the best fit value found in the hottest component. This choice does not introduce any uncertainty given the strong K_{α} line complex of the H-like and He-like iron.
- A set of `mkcflow` models whose minimum and maximum temperatures are fixed in order to cover the 0.3-3.0 keV range with contiguous and not overlapping intervals. Here the normalization of each `mkcflow` component refers to the mass deposition rate in the corresponding temperature interval. The upper and lower temperatures are frozen to the following values: 0.3-0.45, 0.45-0.9, 0.9-1.8 and 1.8-3.0 keV. As in the previous case, a single temperature `mekal` model accounts for the any gas component hotter than 3 keV. Also in this case the redshift is tied to the best-fit found in the hottest component.

As a fitting method, we use the C-Statistics, although we also run our fits with the χ^2 -statistics. In the latter case, spectra are grouped with a minimum signal to noise ratio (S/N) of 4 in each bin. When running C-statistics, we use unbinned spectra (minimum 1 photon per bin). As a default, we consider the energy range 0.5-10 keV both for the MOS and the pn data. We will quote the best fit values with 1σ errorbars on the measured value of \dot{M} , or the 1σ upper limit. The same analysis is applied also to the *Chandra* data for a direct comparison.

4.2. Spectral results on the core region from EPIC MOS and pn data

Before fitting the XMM data, we perform a series of basic tests on our spectra. First, we fit pn and MOS spectra from each exposure separately, using a single `mekal` model, plus the fixed AGN component and Galactic absorption. We find that the best fit temperature values are all consistent within 1σ , showing that all the spectra are broadly consistent with each other. When we add a `mkcflow` component, we notice that the best-fit values of the mass deposition rates from pn data are lower than those from MOS data in all the different exposures. This already shows that there may be significant differences between pn and MOS calibration affecting the measurements of cold gas components. Therefore, we proceed with our standard analysis strategy combining different exposures of the same detector, but fitting pn and MOS spectra separately.

Following our analysis strategy, first we fit separately the MOS and pn data with a single `mkcflow` model, coupled with a `mekal` model to account for the hot ICM along the line of sight. We used both our new XMM-Newton data and the archival data. We consider the energy range 0.5-10 keV both for MOS and pn data. The `XSPEC` version used in this work is v12.8.1.

First we use a single `mkcflow` model with $T_{min} = 0.3 \text{ keV}$ and $T_{max} = 3.0 \text{ keV}$ to fit the combined MOS data with Cash statistics. The redshift of the cold gas component is linked to the best-fit redshift found for the hot component (described by a `mekal` model) $z_X = 0.593 \pm 0.002$, consistent with the optical value (McDonald et al. 2012). We find that the metal abundance of the `mkcflow` component is not constrained by the present data. Therefore we choose to explore the best-fit mass deposition rate by varying the cold gas metallicity Z_{cold} in a wide range of

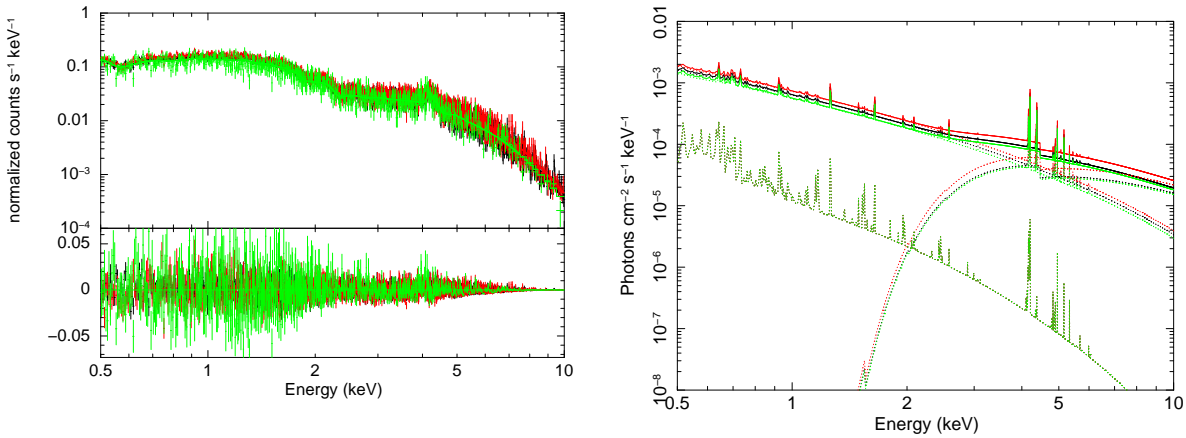


Fig. 3. *Left panel:* MOS spectra from the three Obsid with best-fit model obtained for a single `mckcfow` in the 0.3-3.0 keV temperature range. The lower panel shows the residual with respect to the best-fit model. *Right panel:* components of the best fit model of the MOS spectra (three for each component, shown with dotted lines) obtained for a single `mckcfow` in the 0.3-3.0 keV temperature range. The `mckcfow` component is the lower thermal component, while the AGN contribution is virtually negligible below 2 keV.

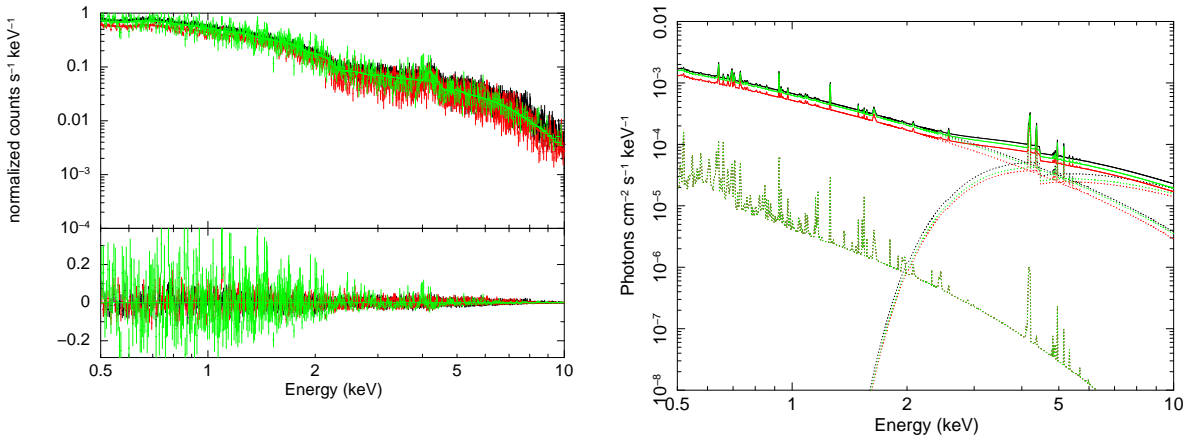


Fig. 4. *Left panel:* pn spectra from the three Obsid with best-fit model obtained for a single `mckcfow` in the 0.3-3.0 keV temperature range. The lower panel shows the residual with respect to the best-fit model. *Right panel:* components of the best fit model of the pn spectra (three for each component, shown with dotted lines) obtained for a single `mckcfow` in the 0.3-3.0 keV temperature range. The `mckcfow` component is the lower thermal component, while the AGN contribution is virtually negligible below 2 keV.

values. We set the minimum value for Z_{cold} equal to the metallicity measured for the hotter `mekal` component $Z_{hot} = 0.47^{+0.04}_{-0.03} Z_{\odot}$ (with solar metallicity values measured by Asplund et al. 2005), and we set the upper limit to the 2σ upper value $\sim 1.4 Z_{\odot}$ found in the inner 80 kpc in the *Chandra* analysis. We quote the best-fit values obtained for $Z_{cold} = 1.0 Z_{\odot}$, and add the uncertainty associated to the range of Z_{cold} as a systematic error. We find a global mass deposition rate $\dot{M} = 620 (-190 + 200)_{stat} (-50 + 150)_{syst} M_{\odot} \text{ yr}^{-1}$. The intrinsic absorption of the AGN is found to be $NH = (42.0 \pm 1.5) \times 10^{22} \text{ cm}^{-2}$, in excellent agreement with the value found with the *Chandra* analysis. The best fit temperature of the hot component is $kT_{hot} = (6.5 \pm 0.3) \text{ keV}$, also in good agreement with the emission weighted temperature in the inner 80 kpc obtained from the analysis of the *Chandra* data. We repeat the fit with χ^2 -statistics binning the spectra to a minimum S/N= 4 per bin, and we find almost identical results, with a reduced $\chi^2 = 1.04$ for 663 dof. The binned spectra of the three Obsid with the best-fit models are shown in Figure 3, left panel. In Figure 3, right panel, we show the different components of the best-fit model. We notice that the contribution of the cold gas in the temperature range 0.3-3 keV is about 5% in the 0.5-1 keV energy band, while the strongly absorbed AGN has virtually no

emission below 2 keV, also when assuming the maximum uncertainty in the intrinsic absorption value. We conclude that the MOS data provides a positive detection of an average mass deposition rate in the temperature range 0.3-3.0 keV at the 3σ c.l., with $\dot{M} > 190 M_{\odot} \text{ yr}^{-1}$ at the 2σ c.l. after considering the systematic effect associated to the unknown metallicity of the cold gas. For completeness, we repeat our analysis without merging MOS1 and MOS2 spectra, therefore combining six spectra from the three exposures. We find comparable results and error bars for all the parameters, with the best fit values for the mass deposition rate lower by 6.5%.

Then we run the multiple `mckcfow` model on the combined MOS spectra. We find that the constraints on the amount of cold gas vary significantly as a function of the temperature range. In this case the metal abundance of the cold gas is linked to the value found in the temperature range 1.8-3.0 keV, which is $Z_{1.8-3\text{keV}} = 0.36^{+0.19}_{-0.15} Z_{\odot}$. The best-fit temperature of the `mekal` component is now $kT_{hot} = 7.4^{+0.5}_{-0.4} \text{ keV}$ with a metal abundance of $Z_{hot} = 0.54^{+0.05}_{-0.04} Z_{\odot}$. The results for \dot{M} are shown in Figure 5, left panel. We notice that the lowest upper limits (at 1σ) are measured in the temperature bins 0.45 – 0.9 and 0.9 – 1.8 keV. These upper limits are providing the strongest constraint for the fit with

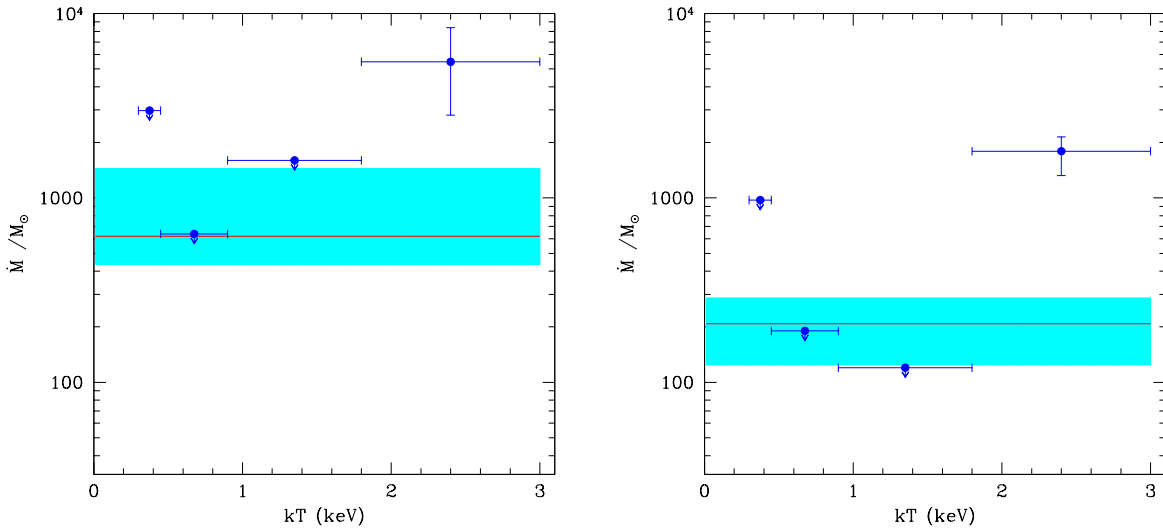


Fig. 5. *Left panel:* mass deposition rate \dot{M} as a function of the temperature from the analysis of the MOS data of the Phoenix with a multi-component `mkcflow` model. Error bars are at 1σ confidence level and arrows represent upper limits at 1σ (the systematic uncertainty is not included here). The red horizontal line shows the best-fit value from the single `mkcflow` model in the 0.3–3.0 keV temperature range, while the shaded area shows the 1σ uncertainty. *Right panel:* Same as in the left panel but for the pn data.

the single `mkcflow` model (see shaded area in Figure 5). We also notice that a clear detection of a mass deposition rate is obtained for the 1.8–3.0 keV temperature range. Therefore, our analysis of the MOS data with a temperature-dependent `mkcflow` model suggests that the cold gas around and below 1 keV is not cooling rapidly as the gas between 2 and 3 keV. This is consistent with the physical conditions often encountered in cool cores, where the gas is cooling down to a temperature floor, below which is hard to probe the presence of cooling gas. However, in the case of the Phoenix the gas is observed to cool down to a temperature much lower than the ambient temperature T_{vir} , as opposed to the classic cool cores where the lowest temperature is $\sim 1/3 T_{vir}$. We remark that we obtained only upper limits on \dot{M} for gas with temperatures below 2 keV. If we compare the results from the multiple `mkcflow` model with that from the single-temperature `mkcflow`, we conclude that the mass deposition rate found in the analysis with a single `mkcflow` model should not be taken as representative of the entire cooling flow, since it is an emission-weighted value averaged over a temperature range which is too wide. Therefore, a temperature-resolved analysis of the cool core structure is mandatory in order to constrain the presence of a cooling flow. Nevertheless, the constraints on the mass deposition rate from MOS data still allow values of several hundreds of $M_\odot \text{ yr}^{-1}$, therefore possibly in agreement with the star formation rate observed in the BCG. Finally, the same fit on the separate MOS1 and MOS2 spectra provides very similar upper limits. In particular, the most constraining bin at $0.45 < kT < 0.90$ keV is left unchanged.

The fit of the pn data with the single `mkcflow` model shows some difficulties. The best fit is obtained when the temperature of the hot component is $kT_{hot} = 5.9 \pm 0.1$ keV, which is in disagreement with the MOS data and with the *Chandra* results. In addition, the reduced $\chi^2 = 1.38$ for 637 degrees of freedom, is significantly larger than the value obtained for the MOS data. The lower temperature of the hot component is enough to account for most of the soft emission which, in the MOS fit, was associated to the cold gas. As a result, the soft emission which

can be associated to the cold gas is significantly lower, and the 3σ upper limit to the mass deposition rate is as low as $\sim 240 M_\odot \text{ yr}^{-1}$.

The significant difference between pn and MOS results clearly requires a detailed treatment of any cross-calibration uncertainty, which is beyond the goal of this paper. A first attempt to estimate the systematic uncertainty due to cross calibration problems is discussed in §4.4. Nevertheless, a reliable assumption which may bring the two analyses in better agreement, is to set the temperature of the hot gas to the value found with *Chandra* and XMM-Newton MOS, $kT_{hot} \sim 6.8$ keV. With this assumption, we find $\dot{M} = 210 (-80 + 85)_{\text{stat}} (-35 + 60)_{\text{syst}} M_\odot \text{ yr}^{-1}$. Also in this case the best fit value has been obtained after freezing the abundance of the cold gas to $Z_{cold} = 1.0 Z_\odot$, and the systematic error has been obtained varying the abundance of the cold gas in the range 0.45–1.4 Z_\odot . The abundance of the hot mekal component is $Z_{hot} = 0.48 \pm 0.04 Z_\odot$ in very good agreement with the MOS data. Finally, also in this case the intrinsic absorption of the AGN is well constrained to be $NH = (43.6 \pm 1.2) \times 10^{22} \text{ cm}^{-2}$. The binned spectra of the three Obsid with the best-fit models are shown in Figure 4, left panel. In Figure 4, right panel, we show the different components of the best-fit model. It is possible to appreciate the lower `mkcflow` component with respect to the right panel of Figure 3. Therefore, we find that the analysis of the pn data plus the condition $kT_{hot} = 6.8$ keV provides a positive detection of a significant mass deposition rate, although about a factor of 3 smaller than those found in the MOS analysis.

We briefly comment on the dependence of \dot{M} on the temperature of the surrounding hot gas. Clearly, the value of \dot{M} critically depends on the amplitude of the continuum and therefore on the hot gas temperature. As already mentioned, our strategy consists in anchoring the hot gas temperature to the best-fit value driven by the continuum in the high energy range, while the colder gas below 3 keV is properly treated by the multi-temperature `mkcflow` model. With present data, any other treatment of the hot gas component would be highly speculative, therefore we do

not further explore the possible impact of the temperature distribution above 3 keV in the cluster core. We argue that the best way to deal with this aspect is to use highly spatially resolved data which allow one to avoid as much as possible the surrounding hot gas component and to focus on the innermost core region.

The analysis with a multi temperature `mkcflow` model, shown in the right panel of Figure 5, confirms this inconsistency. The behaviour of \dot{M} as a function of the temperature is similar, with the most constraining upper limits coming from the temperature bins 0.45 – 0.9 and 0.9 – 1.8 keV and a clear detection of a large mass deposition rate in the 1.8–3.0 keV temperature bin. Also the ratio between \dot{M} in the bin 1.8 – 3.0 keV and the upper limits below 1.8 keV has the same value found in the MOS analysis. Therefore, qualitatively we reach the same conclusion obtained from the MOS data analysis with the multi temperature `mekal` model, but the values \dot{M} are scaled down by a factor ~ 3 . Incidentally, we find that if the energy range used for spectral fitting is reduced to the 0.7–10.0 keV range, best fit values and upper limits from the pn spectra are found in agreement with MOS results. Clearly, this simply depends on the fact that the sensitivity to the cold gas is significantly reduced by excluding the energy bins below 0.7 keV, allowing a much higher upper limits to the contribution from the cold gas.

To summarize, the analysis of XMM-Newton CCD spectra confirms the detection of gas cooling at a rate $> 1000 M_{\odot} \text{ yr}^{-1}$ in the temperature range 1.8–3.0 keV, while it provides only upper limits for gas at temperatures $kT < 1.8 \text{ keV}$. The upper limits to the global mass deposition rate below 1.8 keV appear to be consistent with a SFR of $\sim 800 M_{\odot} \text{ yr}^{-1}$ within 1σ , as measured by McDonald et al. (2013) in the BCG, from the MOS data analysis. On the other hand, the upper limits on \dot{M} measured from pn data at temperatures below 1.8 keV are significantly lower (more than 3σ) than the SFR. Therefore, no definitive conclusion can be drawn on the correspondence between the cooling flow and the observed star formation rate in the core of the Phoenix cluster.

4.3. Spectral results from RGS data

The RGS spectrum is extracted from a strip of roughly 50 arcsec long across the centre of the object, a width corresponding to 90% point spread function (PSF). As the RGS is a slitless instrument and the zero-point of the wavelength calibration is dependent on the position of the detector in the field of view, we use as the source center the coordinates $RA = 23:44:43.9$, $DEC = -42:43:12.64$, which correspond to the position of the central AGN (see §3). In practice, with our choice for the extraction region, we are collecting photons from a box region with dimensions $50'' \times 12'$ centered on the source (see, e.g., Figures 2 and 3 in Werner et al. 2009). This is the standard choice to maximize the signal from the cluster. This choice is motivated also by the fact that the Phoenix cluster has a brightness distribution which is similar to a point source from the XMM point of view, so that the line widening due to the spatial extension of the source is not severely affecting the data. Therefore, the effective area which is sampled by our RGS spectrum is a circle with a radius of $25''$, to be compared with the circle of $13''$ used to extract the EPIC spectra. We also extract an RGS spectrum from a narrower region with dimensions $15'' \times 12'$, corresponding to 70% of the PSF as opposed to the 98% of the PSF achieved with a width of $50''$.

We fit the first-order spectra between 7 and 27 Å, since this is the range where the source is above the background. We used `XSPEC` version 12.8.1 and we use C statistic on the

unbinned spectrum. We first apply a single-temperature `mekal` model modified by the Galactic absorption, while the redshift is fixed at the optical value. The AGN is modeled as in the fits of the EPIC data, however, due to the strongly absorbed spectrum, the effect of the AGN emission is completely negligible in the RGS spectra given the limited wavelength range. From the RGS spectrum extracted from the larger regions (with a width of $50''$) we found that a single temperature model provides a reasonable fit to the data, with a $C_{\text{stat}}/\text{dof} = 1978/1952$ with a best fit temperature of $kT = 6.2 \pm 0.4 \text{ keV}$ with a metal abundance of $Z = 0.55 \pm 0.09 Z_{\odot}$. We show in the left panel of Fig.6 the first-order combined spectrum with the best fitting thermal model. In the same figure we show the positions of relevant emission lines that are clearly identifiable in the spectrum. The set of lines is the same seen in the RGS spectrum of the cluster Abell 1835 as shown in the comparison plot in the right panel of Fig.6. For Abell 1835 we used the same data reduction as performed on the Phoenix data on the three observations not affected by flares (Obsid 0098010101, 0551830101 and 0551830201). The spectrum obtained with our reduction is in very good agreement with the spectrum shown by Sanders et al. (2010). Therefore, from the RGS spectrum of the Phoenix cluster we reach the same conclusions obtained for A1835: no line emission from ionization states below Fe XXIII is seen above 12 Å, and no evidence for gas cooling below $\sim 3 \text{ keV}$ is found.

We then proceed to obtain a measurement of the mass deposition rate from the RGS data by using the `mekal+mkcflow` model with abundances constrained to be the same in both components. As for the EPIC data analysis, the temperature range of the `mkcflow` component is fixed to 0.3 – 3.0 keV. We found no statistically significant improvement with respect to the single temperature model ($C_{\text{stat}}/\text{dof} = 1977/1951$). The best-fit ambient hot temperature is $kT_{\text{hot}} = (6.3 \pm 0.5) \text{ keV}$ with a metal abundance of $Z = 0.43 \pm 0.09 Z_{\odot}$. The best-fit value for the mass deposition rate is $\dot{M} = 122^{+343}_{-122} M_{\odot} \text{ yr}^{-1}$. The 90% upper limit on the mass deposition rate is $682 M_{\odot} \text{ yr}^{-1}$.

More complicated models, such as the one including a set of `mkcflow` models, are not constrained by the RGS data. However, we are able to obtain constraints on the abundance of metals other than iron using a `vmekal` model. We find $Z_{Mg} = (0.53 \pm 0.24) Z_{\odot}$, $Z_{Si} = (0.66 \pm 0.15) Z_{\odot}$, and $Z_S = (0.33 \pm 0.25) Z_{\odot}$. The use of `vmekal` has the effect of providing a slightly lower upper limit on the mass deposition rate: $\dot{M} = 103^{+345}_{-103} M_{\odot} \text{ yr}^{-1}$, with a 90% upper limit of $590 M_{\odot} \text{ yr}^{-1}$. Best-fit temperatures are left unchanged.

We apply the same analysis to the RGS spectrum extracted from a smaller region with a width of $15''$. We obtain very similar results, with small differences, the largest being a smaller value of about 1σ , of the ambient hot temperature, which is measured to be $kT_{\text{hot}} = 5.7^{+0.6}_{-0.3} \text{ keV}$. As for the mass deposition rate, we find a 1σ upper limit of $\dot{M} = 470 M_{\odot} \text{ yr}^{-1}$, with a 90% upper limit at $744 M_{\odot} \text{ yr}^{-1}$. Therefore, we find no difference between the two extraction regions for the RGS spectral analysis.

To summarize, the analysis of the RGS data provide only upper limits to the global mass deposition rate, in agreement with the values found with the analysis of the EPIC pn data, and also consistent with those found with EPIC MOS within less than 2σ . The better agreement with EPIC pn analysis is expected on the basis of the cross-calibration status of XMM instruments: at present the agreement between EPIC pn and RGS is within a few percent, as a result of the combined effect of the RGS contamination model plus the improved pn redistribution model (Stuhlinger 2010).

At the same time, we remark that the comparison between the values of \dot{M} obtained from the two RGS extraction regions and the EPIC pn extraction region, allows us to conclude that our choice of the extraction radius for EPIC data was adequate to sample the possible cold gas emission. The simple fact that \dot{M} from RGS sampled in the region twice larger than that used for EPIC data, is not significantly larger than the value found in the pn data, confirms that no significant emission from cold gas can be found outside the 13" radius.

4.4. Discussion of the systematics in XMM-Newton data analysis

The discrepancy among the results obtained with MOS and pn can be ascribed to the uncertain cross-calibration of the effective area among the XMM-Newton CCD, while there are no other sources of statistical noise which can account for a significant fraction of this discrepancy. This difference is persistent despite the recent model for the MOS contamination introduced in the SAS release v13.5.0 (see Sembay & Saxton 2013). Since the contribution of the cold gas below 3 keV to the total emission in the extracted region is about 3% in the 0.5-2.0 keV energy range, and about 5% in the 0.5-1.0 keV range, an uncertainty in the effective area of the same order may severely affect the measurement of the cold gas.

A first way to estimate the calibration uncertainty is to compare our results with the results obtained applying the correction CORRAREA to the response area of the EPIC detectors based on Read et al. (2014). The CORRAREA calibration is based on an extensive cross-calibration study of 46 non-piled up sources extracted from the 2XMM EPIC Serendipitous Source Catalogue (Watson et al. 2009). This phenomenological correction is meant to bring in agreement the broad-band fluxes measured by EPIC-MOS and EPIC-pn. We can obtain an estimate of the uncertainty on \dot{M} values associated to uncertainties in the EPIC response areas by comparing the best-fit values obtained with and without the CORRAREA correction. We find that the best-fit values of \dot{M} are 1% and 5% higher when applying the CORRAREA correction for MOS and pn data, respectively. This is far from the factor of 3 needed to bring in agreement \dot{M} from MOS and pn. Therefore we conclude that the measurement of cold gas in the spectra of the Phoenix cluster is significantly affected by the calibration of the EPIC detectors, at a level beyond that probed by Read et al. (2014).

We also include the energy range 0.3-0.5 keV to investigate possible effects associated to this low energy band. Despite the calibration is even more uncertain in this range, the inclusion of the lowest energies may help to increase the relative contribution of the cold gas. However, when we repeat our fits on the 0.3-10 keV energy range, we do not find any significant difference with respect to the results described in §4.2.

We also explore the possibility that data taken in different epoch may have different calibration. However, if we exclude the shortest Obsid, acquired two years earlier than most of our data on the Phoenix, the best-fit values are affected only by a negligible amount.

A major source of uncertainty in the soft band is the Galactic column density. The possible presence of unnoticed fluctuations in the Galactic neutral hydrogen column densities on scales smaller than the resolution of Kalberla et al. (2005) may reach 10-40% on scales of ~ 1 arcmin (Barnes & Nulsen 2003). Therefore, we consider a systematic uncertainty in our best-fit values of \dot{M} assuming a maximum variation of NH_{Gal} by 40%. The typical effect is that the best fit is obtained for the maxi-

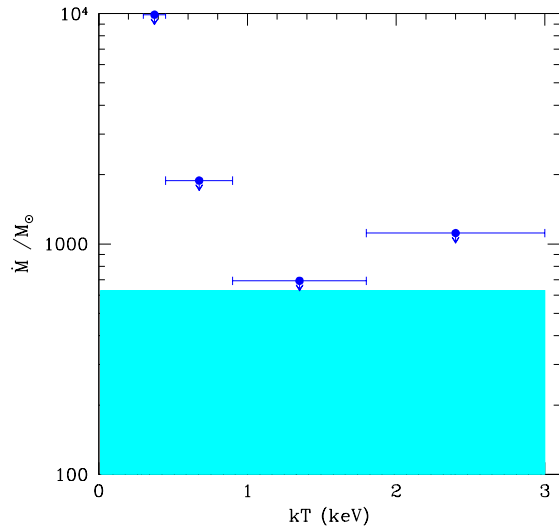


Fig. 7. Mass deposition rate \dot{M} as a function of the temperature from the analysis of the ACIS-I *Chandra* data of the Phoenix within 30 kpc from the center. The AGN emission has been removed (inner 1.5 arcsec). The results have been obtained with a multi-temperature `mkcflow` plus a `mekal` model for the hot component. Arrows refer to 1 σ upper limits. Shaded area shows the 1 σ upper limit based on the analysis of a single `mkcflow` model in the 0.3-3.0 keV temperature range plus a `mekal` model for the hot component.

num allowed value of NH_{Gal} , and this implies that much more cold gas can be allocated. Specifically, if we allow the Galactic absorption to vary up to $NH_{Gal} = 2.13 \times 10^{20} \text{ cm}^{-2}$, we find $\dot{M} = 900(-390 + 110)_{\text{stat}}(-130 + 250)_{\text{syst}} M_{\odot} \text{ yr}^{-1}$ from the analysis of the MOS data with a single `mkcflow` model in the temperature range 0.3-3.0 keV. This value is 45% larger than that obtained with the NH_{Gal} value of Kalberla et al. (2005) at the position of the cluster. Similar effect is found for the other fits, including those with the multi-component `mkcflow` model. If, on the other hand, we leave NH_{Gal} free to vary, we find a best fit values of $NH_{bestfit} = (2.2 \pm 0.8) \times 10^{20} \text{ cm}^{-2}$, very close to the upper bound we assumed for NH_{Gal} . The analysis of the EPIC pn data, with the same values of NH_{Gal} , provides \dot{M} values 2.3 and 3 times larger for $NH_{Gal} = 2.13$ and $2.2 \times 10^{20} \text{ cm}^{-2}$, respectively, thus considerably reducing the discrepancy between MOS and pn analysis. However, when the Galactic absorption is left free, the best-fit value is $NH_{Gal} = (0.8 \pm 0.2) \times 10^{20} \text{ cm}^{-2}$, which, in turn, provides much lower values of \dot{M} with respect to the standard analysis. Therefore, we conclude that there are no hints for a plausible variation of NH_{Gal} which can significantly change our results, including the discrepancy between the best-fit values of \dot{M} found between MOS and pn data.

4.5. Comparison with spectral results on the core region from *Chandra* data

We repeat the same fits on the *Chandra* data available in the archive as of December 2014. The photometry in the inner 30 kpc, corresponding to 4.5 arcsec, excluding the central AGN, amounts to 1510 net counts in the 0.5 – 7.0 keV energy band. This is usually not sufficient to provide robust constraints on the

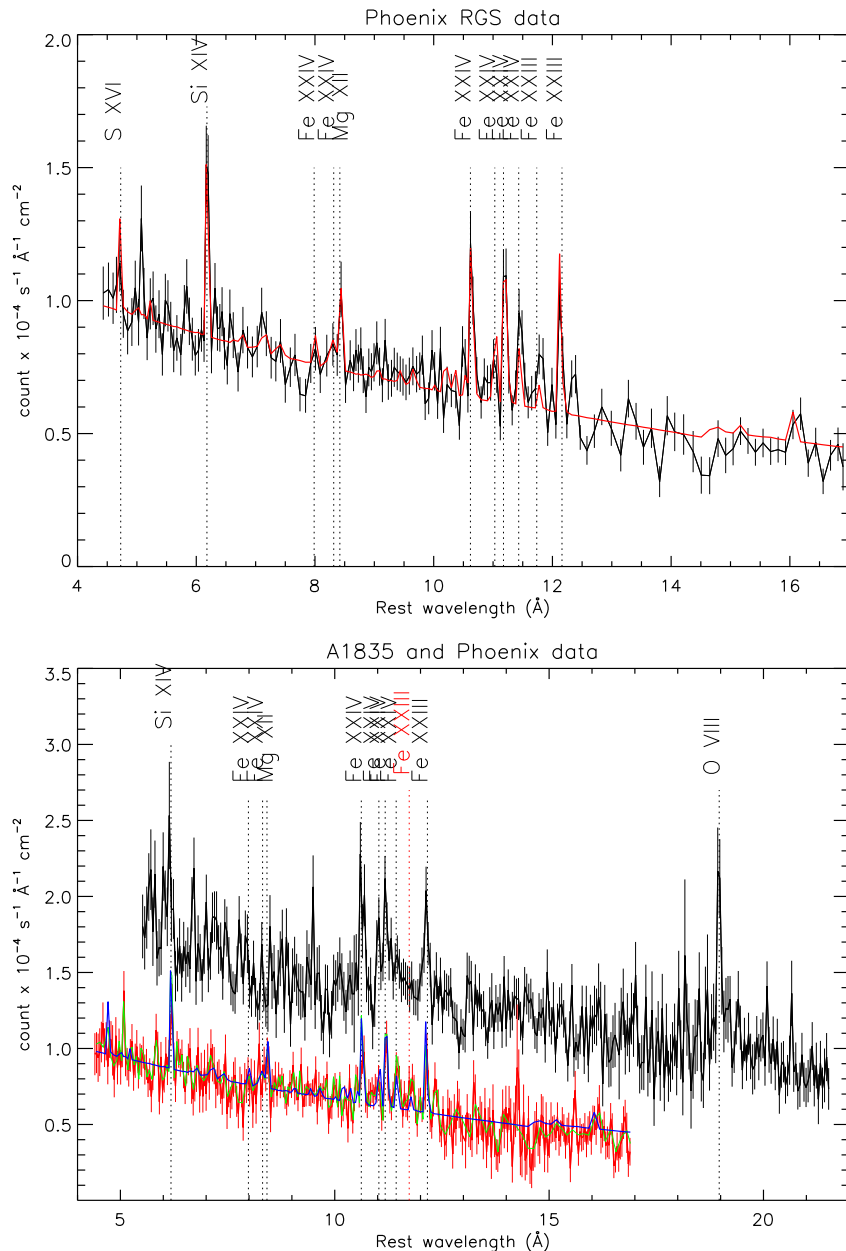


Fig. 6. *Top panel:* combined RGS 1 and 2 spectrum for the Phoenix cluster and best-fit, single-temperature model. The data have been rebinned to have a signal to noise of 10 and divided by the effective area of the instrument only for displaying purpose. Relevant lines are also labeled. *Bottom panel:* The Phoenix spectrum (in red) is compared with the RGS spectrum of Abell 1835 (in black). We plot the fluxed spectra obtained with RGSFLUXER. Similar results are obtained by plotting the unfolded spectrum in *XSPEC* (the green line in the Phoenix spectrum) wit the only difference set by the binning condition $S/N = 10$. The best-fit thermal model of the Phoenix is also plotted as a blue line. We also plot relevant lines clearly seen in the spectra: the same set of line are present in both spectra in the overlapping wavelength range.

amount of cold gas in nearby clusters, and it would be even less effective at the redshift of the Phoenix. Nevertheless, we perform our spectral analysis as for the XMM-Newton data. The single `mkcflow` model in the temperature range 0.3–3.0 keV provides a 1σ upper limit of $630(-85 + 60)_{\text{syst}}$ $M_{\odot} \text{ yr}^{-1}$ or a 2σ upper limit of $1130(-150 + 1100)_{\text{syst}}$ $M_{\odot} \text{ yr}^{-1}$, where the systematic uncertainty corresponds to $0.45 < Z_{\text{cold}} < 1.4 Z_{\odot}$. The hot gas temperature is $kT_{\text{hot}} = 7.2^{+1.3}_{-0.6}$ keV, within 1σ from the value found in XMM-Newton analysis and in the overall temperature profile of the *Chandra* data. We remind the reader that we do

not fit the AGN since its emission has been removed from the spectrum thanks to the *Chandra* angular resolution.

Despite the low S/N of the *Chandra* data (almost two orders of magnitude less photons with respect to the combined XMM-Newton spectra), and the high redshift of the Phoenix cluster, we also perform the fit with a multi-component `mkcf` flow model. Temperature and metallicity of the hot gas component are the same as in the previous fit, while $Z_{cold} = 1.0 Z_{\odot}$. As expected, we obtain little additional information. The results are summarized in Figure 7, where we can conclude that the strongest con-

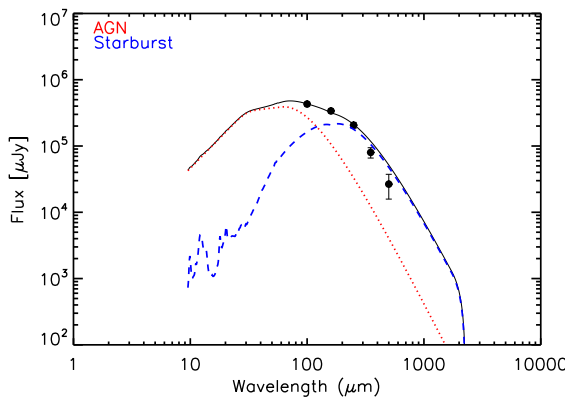


Fig. 8. Spectral energy distribution of the BCG of the Phoenix in the far-infrared (FIR) from the PACS (100 and 160 μm) and SPIRE (250, 350, 500 μm) instruments on board the *Herschel* Space Observatory. The red dotted line and the blue dashed line show the best-fit to the SED for the AGN and starburst template, respectively.

straints on \dot{M} comes mostly from the gas between 0.9 and 1.8 keV. Therefore, *Chandra* upper limits are consistent with a mass deposition rate of the order of $\sim 1000 M_{\odot} \text{ yr}^{-1}$. We remark, however, that deeper *Chandra* data are expected to provide much stronger constraints.

5. Exploring the connection between SFR and global \dot{M}

We inspected available FIR data on the Phoenix in order to better constrain the SFR. The BCG has been observed in the far-infrared (FIR) with the PACS (100 and 160 μm) and SPIRE (250, 350, 500 μm) instruments on board the *Herschel* Space Observatory (Pilbratt et al. 2010). *Herschel* data bracket the critical peak of FIR emission of high-redshift galaxies, providing a direct, unbiased measurement of the dust-obscured star-formation. We perform aperture photometry assuming an aperture radius of 6 and 9 arcsec for 100 and 160 μm , respectively, while for SPIRE we used PSF fitting. The five data points from *Herschel* instruments provide the spectral energy distribution (SED) shown in Figure 8.

We investigate the contribution of the AGN component to the FIR emission using the program DECOMPIR (Mullaney et al. 2011), a SED-model-fitting software that aims to separate the AGN from the host star-forming (SF) galaxy. The AGN component is an empirical model based on observations of local AGNs, whereas the five starburst models were developed to represent a typical range of SED types, with an extrapolation beyond 100 μm using a grey body with emissivity β fixed to 1.5. The best-fitting model obtained with DECOMPIR confirms at least a 50% contribution of the AGN to the total SED flux, as shown in Figure 8. The AGN clearly dominates the FIR emission. The IR luminosity for the starburst component (best described by the model SB5 in Mullaney et al. 2011) is measured to be $L_{\text{IR}} = 3.1 \times 10^{12} L_{\odot}$. Assuming a Salpeter IMF, this luminosity corresponds to a star formation rate of $530 M_{\odot} \text{ yr}^{-1}$ with a typical error of 15%, therefore lower than the value found by McDonald et al. (2013) at 3σ c.l. The total luminosity given by the best-fit is $L_{\text{IR}} = 2.09 \times 10^{13} L_{\odot}$, with the AGN component contributing by 86%. Taken at face value, this revised estimate

of the SFR is in excellent agreement with the mass deposition rate found with the analysis of the EPIC MOS data, while is still inconsistent at about 3σ c.l. with the mass deposition rate found with EPIC pn analysis.

6. Conclusions

We analyzed the X-ray data taken with a 220 ks exposure of XMM–Newton on the Phoenix cluster. We focus on the presence of cold gas in the core by selecting a circle of 13.5 arcsec centered on the BCG in the XMM image and a strip with a width corresponding to 90% of the PSF in the RGS data. Our immediate goal is to constrain the actual mass deposition rate associated with the residual cooling flow, with the aim of understanding whether this may be directly linked to the current massive starburst observed in the BCG. We combine XMM–Newton data with shallow *Chandra* data, particularly to model the hard emission of the central absorbed AGN, which cannot be removed from the XMM–Newton data alone. Our results are summarized as follows:

- we measure an average mass deposition rate of $\dot{M} = 620 (-190 + 200)_{\text{stat}} (-50 + 150)_{\text{syst}} M_{\odot} \text{ yr}^{-1}$ and $\dot{M} = 210 (-80 + 85)_{\text{stat}} (-35 + 60)_{\text{syst}} M_{\odot} \text{ yr}^{-1}$ in the 0.3–3.0 keV temperature range from the analysis of the MOS and pn data, respectively. These values are dominated by the cold gas in the energy range 1.8–3.0 keV, while only upper limits can be obtained at temperatures below 1.8 keV. Therefore, the upper limits to the global mass deposition rate below 1.8 keV appear to be consistent with a SFR of $\sim 800 M_{\odot} \text{ yr}^{-1}$, as measured in the BCG by McDonald et al. (2013), from the EPIC MOS data analysis within 1σ), while the upper limits on \dot{M} measured from EPIC pn data at temperatures below 1.8 keV are significantly lower (more than 3σ) than the SFR measured in McDonald et al. (2013).
- If we focus on the temperature range 0.3–1.8 keV, we find that MOS data analysis is consistent with $\dot{M} \sim 1000$ within 1σ , while the pn data provide $\dot{M} < 400 M_{\odot} \text{ yr}^{-1}$ at 3σ c.l.
- Since the discrepancy between the MOS and pn data analyses cannot be explained on the basis of currently known cross-calibration uncertainties between the two instruments nor of other sources of statistical noise, we argue that further calibration issues between EPIC instruments still need to be understood and properly treated. Indeed, the contribution of the cold gas with an average mass deposition rate of $\sim 600 M_{\odot} \text{ yr}^{-1}$ in the EPIC data is about 5% in the energy range 0.5–1.0 keV for our extraction region. This implies that any calibration uncertainty of the same order strongly affects the data. This conclusion is valid in the framework of the isobaric cooling model which we assumed in this paper. At present, we are not able to discuss whether the assumptions of different physical models to describe the cooling of the gas can change the picture and impact on the difference between MOS and pn analysis.
- In the RGS spectrum, no line emission from ionization states below Fe XXIII is seen above 12 Å, and the amount of gas cooling below ~ 3 keV has a formal best-fit value for the mass deposition rate of $\dot{M} = 122^{+343}_{-122} M_{\odot} \text{ yr}^{-1}$. This result is confirmed by a direct comparison of the Phoenix RGS spectrum with A1835 in the overlapping spectral range. Therefore, the mass deposition rate from RGS analysis is lower than the SFR of McDonald et al. (2013) in the BCG at the 2σ c.l.

- Current *Chandra* data (from a short exposure of ~ 10 ks) are in agreement with our XMM-Newton analysis, but do not provide meaningful constraints on \dot{M} . Deeper *Chandra* data, thanks to the high angular resolution, are expected to provide tighter constraints to the global mass deposition rate.
- A careful analysis of the FIR SED based on *Herschel* data provides a value for the SFR in the BCG of $530 M_{\odot} \text{ yr}^{-1}$ with an uncertainty of 15%. This revised estimate of the SFR is in very good agreement with the \dot{M} from EPIC MOS data and consistent within 1σ with \dot{M} from the RGS analysis, while still inconsistent at more than 3σ with the mass deposition rate found in EPIC pn data. Therefore, our revised SFR is not changing significantly the comparison between SFR and the global \dot{M} in the Phoenix cluster.

To summarize, the range of \dot{M} allowed by XMM-Newton data from EPIC MOS is consistent with the SFR observed in the BCG, while EPIC pn and RGS data analysis suggest a mass deposition rate of the order of $\sim SFR/3$, and the derived upper limit is inconsistent with the observed SFR at least at the 2σ level for RGS, and more than 3σ for EPIC-pn. As a consequence, the results described in this work do not provide a final answer on the possible agreement between the mass deposition rate of isobaric cooling gas in the core and the observed SFR in the BCG. As recently shown by Molendi et al. (in preparation), \dot{M} is often measured to be significantly lower than the global SFR in central cluster regions for several strong cool-core clusters. These findings suggest that cooling flows may be short-lived episodes, efficient in building the cold mass reservoir that, on a different time scale, and possibly with some delay, triggers the star formation rate in the BCG. To investigate whether this occurs also in the Phoenix cluster, or whether the Phoenix actually hosts the largest cooling flow observed so far with $\dot{M} \simeq SFR$, we must wait for deep, high-resolution, spatially resolved X-ray spectral analysis, in order to remove as much as possible the stronger emission from the surrounding hot gas.

Acknowledgements. We acknowledge financial contribution from contract PRIN INAF 2012 (“A unique dataset to address the most compelling open questions about X-ray galaxy clusters”). IB and JSS acknowledge funding from the European Union Seventh Framework Programme (FP7/2007-2013) under grant agreement no. 267251 “Astronomy Fellowships in Italy” (AstroFlit). We thank Guido Risaliti for useful discussions on the XMM data reduction and analysis. We also thank the anonymous Referee for comments and suggestions which significantly improved the paper.

References

Arnaud, M., Pratt, G. W., Piffaretti, R., et al. 2010, A&A, 517, A92

Asplund, M., Grevesse, N., & Sauval, A. J. 2005, in Astronomical Society of the Pacific Conference Series, Vol. 336, Cosmic Abundances as Records of Stellar Evolution and Nucleosynthesis, ed. T. G. Barnes III & F. N. Bash, 25

Barnes, D. G. & Nulsen, P. E. J. 2003, MNRAS, 343, 315

Blanton, E. L., Randall, S. W., Clarke, T. E., et al. 2011, ApJ, 737, 99

Böhringer, H., Belsole, E., Kennea, J., et al. 2001, A&A, 365, L181

Böhringer, H., Matsushita, K., Churazov, E., Ikebe, Y., & Chen, Y. 2002, A&A, 382, 804

Cowie, L. L. & Binney, J. 1977, ApJ, 215, 723

De Grandi, S., Santos, J. S., Nonino, M., et al. 2014, A&A, 567, A102

Ettori, S., Donnarumma, A., Pointecouteau, E., et al. 2013a, Space Sci. Rev., 177, 119

Ettori, S., Gastaldello, F., Gitti, M., et al. 2013b, A&A, 555, A93

Ettori, S., Gastaldello, F., Leccardi, A., et al. 2010, A&A, 524, A68

Fabian, A. C. 1994, ARA&A, 32, 277

Fabian, A. C. & Nulsen, P. E. J. 1977, MNRAS, 180, 479

Fabian, A. C., Sanders, J. S., Allen, S. W., et al. 2011, MNRAS, 418, 2154

Fabian, A. C., Sanders, J. S., Allen, S. W., et al. 2003, MNRAS, 344, L43

Fabian, A. C., Sanders, J. S., Taylor, G. B., et al. 2006, MNRAS, 366, 417

Gaspari, M., Brighenti, F., D’Ercole, A., & Melioli, C. 2011a, MNRAS, 415, 1549

Gaspari, M., Melioli, C., Brighenti, F., & D’Ercole, A. 2011b, MNRAS, 411, 349

Gonzalez, A. H., Sivanandam, S., Zabludoff, A. I., & Zaritsky, D. 2013, ApJ, 778, 14

Kaastra, J. S., Ferrigno, C., Tamura, T., et al. 2001, A&A, 365, L99

Kalberla, P. M. W., Burton, W. B., Hartmann, D., et al. 2005, A&A, 440, 775

Kirkpatrick, C. C., McNamara, B. R., & Cavagnolo, K. W. 2011, ApJ, 731, L23

Komatsu, E., Smith, K. M., Dunkley, J., et al. 2011, ApJS, 192, 18

Lin, Y.-T., Mohr, J. J., & Stanford, S. A. 2003, ApJ, 591, 749

Mathews, W. G. & Bregman, J. N. 1978, ApJ, 224, 308

Mazzotta, P., Rasia, E., Moscardini, L., & Tormen, G. 2004, MNRAS, 354, 10

McDonald, M., Bayliss, M., Benson, B. A., et al. 2012, Nature, 488, 349

McDonald, M., Benson, B., Veilleux, S., Bautz, M. W., & Reichardt, C. L. 2013, ApJ, 765, L37

McNamara, B. R. & Nulsen, P. E. J. 2012, New Journal of Physics, 14, 055023

McNamara, B. R., Nulsen, P. E. J., Wise, M. W., et al. 2005, Nature, 433, 45

McNamara, B. R., Wise, M., Nulsen, P. E. J., et al. 2000, ApJ, 534, L135

Molendi, S. & Pizzolato, F. 2001, ApJ, 560, 194

Mullaney, J. R., Alexander, D. M., Goulding, A. D., & Hickox, R. C. 2011, MNRAS, 414, 1082

Mushotzky, R. F. & Szymkowiak, A. E. 1988, in NATO ASIC Proc. 229: Cooling Flows in Clusters and Galaxies, ed. A. C. Fabian, 53–62

Navarro, J. F., Frenk, C. S., & White, S. D. M. 1996, ApJ, 462, 563

Peterson, J. R. & Fabian, A. C. 2006, Phys. Rep., 427, 1

Peterson, J. R., Kahn, S. M., Paerels, F. B. S., et al. 2003, ApJ, 590, 207

Peterson, J. R., Paerels, F. B. S., Kaastra, J. S., et al. 2001, A&A, 365, L104

Pilbratt, G. L., Riedinger, J. R., Passvogel, T., et al. 2010, A&A, 518, L1

Randall, S. W., Forman, W. R., Giacintucci, S., et al. 2011, ApJ, 726, 86

Read, A. M., Guainazzi, M., & Sembay, S. 2014, A&A, 564, A75

Sanders, J. S., Fabian, A. C., Smith, R. K., & Peterson, J. R. 2010, MNRAS, 402, L11

Santos, J. S., Tozzi, P., Rosati, P., & Böhringer, H. 2010, A&A, 521, A64

Santos, J. S., Tozzi, P., Rosati, P., Nonino, M., & Giovannini, G. 2012, A&A, 539, A105

Sembay, S. & Saxon, R. 2013, XMM-CCF-REL-0305

Silk, J. 1976, ApJ, 208, 646

Stuhlinger, M. 2010, XMM-SOC-CAL-TN-0052

Sun, M. 2009, ApJ, 704, 1586

Tamura, T., Kaastra, J. S., Peterson, J. R., et al. 2001, A&A, 365, L87

Ueda, S., Hayashida, K., Anabuki, N., et al. 2013, ApJ, 778, 33

Watson, M. G., Schröder, A. C., Fyfe, D., et al. 2009, A&A, 493, 339

Werner, N., Zhuravleva, I., Churazov, E., et al. 2009, MNRAS, 398, 23

Williamson, R., Benson, B. A., High, F. W., et al. 2011, ApJ, 738, 139

Zhuravleva, I., Churazov, E., Schekochihin, A. A., et al. 2014, Nature, 515, 85